

# Adaptive information-maximization encoding for ghost imaging—A general Bayesian framework under experimental physical constraints

Jianshuo Sun<sup>1,2,3</sup>, Chenyu Hu<sup>1\*</sup>, Zunwang Bo<sup>2,3</sup>, Zhentao Liu<sup>2,3</sup>, Mengyu Chen<sup>2,3</sup>, Longkun Du<sup>4</sup>, Weitao Liu<sup>5</sup>, Shensheng Han<sup>1,2,3\*</sup>

<sup>1</sup>\*School of Physics and Optoelectronic Engineering, Hangzhou Institute for Advanced Study, University of Chinese Academy of Sciences, Hangzhou, 310024, Zhejiang, China.

<sup>2</sup>Aerospace Laser Technology and System Department, Shanghai Institute of Optics and Fine Mechanics, Chinese Academy of Sciences, Shanghai, 201800, China.

<sup>3</sup>Center of Materials Science and Optoelectronics Engineering, University of Chinese Academy of Sciences, Beijing, 100049, China.

<sup>4</sup>State Key Laboratory of Chemistry for NBC Hazards Protection, PLA AMS, Beijing, 102205, China.

<sup>5</sup>College of Science, National University of Defense Technology, Changsha, 410073, Hunan, China.

\*Corresponding author(s). E-mail(s): [huchenyu@ucas.ac.cn](mailto:huchenyu@ucas.ac.cn);  
[sshan@mail.shcnc.ac.cn](mailto:sshan@mail.shcnc.ac.cn);

## Abstract

Ghost imaging (GI) has demonstrated diverse imaging capabilities enabled by its encoding-decoding-based computational imaging mechanism. Accordingly, information-theoretic studies have emerged as a promising avenue for probing the fundamental performance bounds of GI and related computational imaging paradigms. However, the design of information-theoretically optimal encoding strategies remains largely unexplored, primarily due to the intractability of the prior probability density function (PDF) of an unknown scene. Here, by leveraging the ability of recursively estimating the PDF of the object to be imaged via Bayesian filtering, we propose to establish an adaptive information-maximization encoding (AIME) design framework. Based on the adaptively estimated posterior PDF from previously acquired measurements, the expected information gain of

subsequent detections is evaluated and maximized to design the corresponding encoding patterns in a closed-loop manner. Within this framework, the theoretical form of the information-optimal encoding under representative physical constraints is analytically derived. Corresponding experimental results show that, GI systems employing information-optimal encoding achieve markedly improved imaging performance compared with conventional fixed point-to-point imaging without relying on additional heuristic regularization schemes, particularly in low signal-to-noise ratio regimes. Moreover, the proposed strategy consistently enables significantly enhanced information acquisition capability compared with existing encoding strategies, leading to substantially improved imaging quality. These results establish a principled information-theoretic foundation for optimal encoding design in computational imaging paradigms, provided that the forward model can be accurately characterized.

## 1 Introduction

Ghost imaging (GI) [1] has demonstrated a broad range of capabilities, including acquisition of high-dimensional (H-D) information through low-dimensional detection [2], enhancement of two-dimensional resolution via H-D light-field information [3, 4], non-locally decoupling detection efficiency and imaging resolution [5], and reduction of the unnecessary detection redundancy [6]. These advantages have enabled its diverse applications in imaging LiDAR [7, 8], single-shot H-D imaging cameras [9, 10], super-resolution microscopy [11, 12], low-dose and multi-dimensional radiographic imaging [13, 14], imaging in special band [15, 16], and task-oriented imaging [17, 18]. From the perspective of imaging information acquisition [19, 20], GI can be interpreted as an encoding-decoding-based computational imaging paradigm [21], where the imaging object is encoded by randomly fluctuating light fields, and the desired image is decoded through high-order light-field correlation. This formulation naturally places GI within an information-theoretic framework, under which analyses of information acquisition efficiency and fundamental performance are in principle attainable [22–24].

Within the information-theoretic framework, a fundamental question in GI, and more broadly in such computational imaging paradigms, concerns the existence and design of information-theoretically optimal encoding [25]. In information theory, the encoding optimality is commonly evaluated using information-content measures, such as mutual information [26] and Fisher information [27]. However, the probability density function (PDF) of the object to be imaged, which is required for calculating these information measures, is generally intractable in practical imaging systems. As a result, information-theoretic studies on encoding design of GI have so far been confined to very restrictive assumptions or special scenarios [22] rather than a general imaging scenario. As a practical compromise, encoding optimization has been extensively explored within the framework of compressed sensing (CS), motivated by the principle that incoherent sampling can preserve the information of sparse signals with high efficiency [28]. Assuming sparsity of the image in a specific transform domain, the encoding patterns in GI can be optimized by minimizing mutual coherence of the

sensing matrix [6, 29, 30]. Nevertheless, such CS-based framework typically neglect the influence of measurement noise, as exact recovery guarantees are theoretically established only in the noiseless case [31]. In practical scenarios, the detection noise is often amplified [32] in related image retrieval, rendering signal recovery particularly challenging in the low signal-to-noise ratio (SNR) regime. Thus, existing approaches along this line remain theoretically incomplete, and are difficult to apply to GI under realistic low-SNR conditions.

Recently, by modeling the linear computational imaging system within the Bayesian filtering framework, Du *et al.* [33] proposed a recursive approach to estimate the PDF of the imaging object from already-acquired detection signals. This formulation suggests a promising route for evaluating information-theoretic measures and designing information-optimal encoding light fields in an adaptive manner. However, from existing studies on adaptive GI [34, 35], it remains unclear whether adaptive measurements can consistently yield fundamental performance gains, particularly from an information-theoretic perspective. More broadly, in the context of adaptive CS, the superiority of adaptive sensing over non-adaptive measurements has long remained theoretically inconclusive [36–38], especially in noisy and practically constrained regimes.

In this Article, we explicitly investigate the possibility to adaptively establish the information-optimal encoding for GI, and propose a general adaptive information-maximization encoding (AIME) framework. It enables quantitative evaluation of the information content acquired in the encoding-detection process, and facilitates the design of optimal encoding under practical constraints through information maximization. Theoretical analysis and numerical simulations consistently show that, under a total-energy constraint corresponding to a fixed encoding illumination energy, the information-maximization encoding converges to a point-like illumination pattern. In contrast to traditional imaging, the resulting scanning order is adaptively determined by the object rather than following a deterministic sequence. Owing to this adaptive design, the proposed AIME strategy achieves superior imaging performance compared to conventional “fixed point-to-point” imaging mode without relying on additional heuristic regularization schemes, particularly in low signal-to-noise ratio (SNR) regimes. Comparison with typical encoding patterns also show that the information-optimal encoding consistently yields improved imaging quality across a wide range of sampling ratios (SRs) and SNR conditions. The proposed framework establishes a principled information-theoretic foundation for characterizing and approaching the fundamental performance of computational imaging paradigms.

## 2 Results

### 2.1 Principle of AIME for GI

We formulate AIME as a closed-loop information-theoretic framework for GI, in which the encoding patterns are treated as variables to be optimized according to the evolving statistical state of the estimated imaging object. As illustrated in Fig. 1, at each measurement step, the statistical state is represented by a posterior PDF inferred from previously detected signals, based on which the expected information gain of

a candidate encoding is evaluated. The subsequent encoding is then determined by maximizing the information criterion under explicit physical followed by a recursive update of the posterior PDF after measurement. Within this formulation, encoding, detection, and statistical inference in GI are integrated into a unified framework, enabling information-optimal encoding to be defined and implemented sequentially without requiring special assumption on prior knowledge of the object statistics.

### 2.1.1 Bayesian formulation for recursive posterior PDF tracking

To enable information-theoretic evaluation and optimization of encoding, the statistical state of the imaging object is characterized by a posterior PDF that is updated recursively as measurements are acquired. To this end, the forward encoding-detection process of GI is formulated to construct the measurement-likelihood function  $p(\mathbf{z} | \mathbf{x})$ , specifically as [21]

$$\mathbf{z} = \beta \mathbf{Hx} + \mathbf{n}, \quad (1)$$

where  $\mathbf{z}$  stands for the recorded signal,  $\mathbf{x}$  denotes the desired object's image,  $\mathbf{H}$  is the measurement matrix consisting of the encoding light fields  $\{\mathbf{h}_1, \mathbf{h}_2, \dots, \mathbf{h}_K\}^\top$  with  $K$  being the number of acquired measurements,  $\mathbf{n}$  is the detection noise, and  $\beta$  represents a coefficient accounting for various system-dependent factors. This formulation is also shared by a broad class of computational imaging systems.

Then, an initial Gaussian distribution  $p(\mathbf{x} | \mathbf{Z}_0) = p_0(\mathbf{x}) = \mathcal{N}(\hat{\mathbf{x}}_0, \hat{\mathbf{P}}_0)$  is assumed. By considering the forward sub-model with a frame of light fields  $\mathbf{h}_k$  constructed as  $p(\mathbf{z}_k | \mathbf{x}) = \mathcal{N}(\beta \mathbf{h}_k^\top \mathbf{x}, R_k)$ , the posterior PDF after the  $k$ -th measurement is obtained as

$$p(\mathbf{x} | \mathbf{Z}_k) = \mathcal{N}(\hat{\mathbf{x}}_k, \hat{\mathbf{P}}_k). \quad (2)$$

Here a Gaussian approximation  $n_k \sim \mathcal{N}(0, R_k)$  for the noise model is adopted, where  $R_k = \beta \mathbf{h}_k^\top \hat{\mathbf{x}}_{k-1}$  results from the photon noise assumption, with the current estimate  $\hat{\mathbf{x}}_{k-1}$  used to approximate the unknown true  $\mathbf{x}$ . Under these settings, the posterior statistics  $\hat{\mathbf{x}}_k$ ,  $\hat{\mathbf{P}}_k$  are obtained via recursive expressions

$$\hat{\mathbf{x}}_k = \hat{\mathbf{x}}_{k-1} + \mathbf{K}_k (\mathbf{z}_k - \beta \mathbf{h}_k^\top \hat{\mathbf{x}}_{k-1}), \quad (3a)$$

$$\hat{\mathbf{P}}_k = (\mathbf{I} - \beta \mathbf{K}_k \mathbf{h}_k^\top) \hat{\mathbf{P}}_{k-1}, \quad (3b)$$

with

$$\mathbf{K}_k = \beta \hat{\mathbf{P}}_{k-1} \mathbf{h}_k (\beta^2 \mathbf{h}_k^\top \hat{\mathbf{P}}_{k-1} \mathbf{h}_k + R_k)^{-1}.$$

These posterior statistics serve as sufficient descriptors of the statistical state and provide the basis for quantitatively assessing the information content of subsequent measurements, as will be used in the following subsection.

### 2.1.2 Theoretical objective of AIME

Based on the posterior PDF  $p(\mathbf{x} | \mathbf{Z}_k)$  obtained from recursive inference, the encoding for the  $(k+1)$ -th measurement can be formulated as a variable to be optimized according to an information-theoretic criterion. In the AIME framework, this optimization is guided by the expected reduction of posterior uncertainty induced by

a candidate encoding, which provides a principled definition of information-optimal encoding. Here, the mutual information and the Fisher-information-related criterion are employed as two representative information-theoretic measures of this principle.

- **The mutual information** between the  $k$ -th detection signal and the imaging object  $I(z_k, \mathbf{x} | \mathbf{Z}_{k-1})$  is calculated by

$$I(\mathbf{z}_k, \mathbf{x} | \mathbf{Z}_{k-1}) = \int d\mathbf{z}_k d\mathbf{x} p(\mathbf{z}_k, \mathbf{x} | \mathbf{Z}_{k-1}) \log \frac{p(\mathbf{z}_k, \mathbf{x} | \mathbf{Z}_{k-1})}{p(\mathbf{z}_k)p(\mathbf{x} | \mathbf{Z}_{k-1})} \quad (4)$$

and obtained as

$$I(\mathbf{z}_k, \mathbf{x} | \mathbf{Z}_{k-1}) = \frac{1}{2} \log \frac{1}{|\mathbf{I} - \beta \mathbf{K}_k \mathbf{h}_k^\top|} = \frac{1}{2} \log \left( 1 + \beta^2 \frac{\mathbf{h}_k^\top \hat{\mathbf{P}}_{k-1} \mathbf{h}_k}{R_k} \right). \quad (5)$$

Hence, maximizing the mutual information is equivalent to maximizing the following objective

$$\mathcal{L}_{\text{MI}} = \frac{\mathbf{h}_k^\top \hat{\mathbf{P}}_{k-1} \mathbf{h}_k}{R_k}. \quad (6)$$

For convenience, this mutual-information-based formulation is hereafter referred to as AIME-MI.

- **The Fisher information** contained in the detection signal  $z_k$  is in fact represented by the Fisher information matrix (FIM)  $\hat{\mathbf{P}}_k^{-1}$  [33]. Since the calculation of matrix inverse is time-consuming, instead of FIM, here the Cramér-Rao bound (CRB) is applied to perform the information-optimal encoding design by minimizing it. Specifically, the mean CRB (mCRB) which stand for the error bound averaging on all pixels of the imaging object is calculated by

$$\text{mCRB} = \text{Tr}(\hat{\mathbf{P}}_k) \quad (7)$$

and obtain as

$$\text{mCRB} = \text{Tr}(\hat{\mathbf{P}}_{k-1}) - \frac{\mathbf{h}_k^\top \hat{\mathbf{P}}_{k-1}^2 \mathbf{h}_k}{\mathbf{h}_k^\top \hat{\mathbf{P}}_{k-1} \mathbf{h}_k + \frac{R_k}{\beta^2}}. \quad (8)$$

Since the covariance matrix  $\hat{\mathbf{P}}_{k-1}$  has been determined by already-acquired detection, to minimize the mean CRB, only the last term in Eq. (8) can be optimized. Hence, minimizing the mCRB is equivalent to maximizing the following objective

$$\mathcal{L}_{\text{CRB}} = \frac{\mathbf{h}_k^\top \hat{\mathbf{P}}_{k-1}^2 \mathbf{h}_k}{\mathbf{h}_k^\top \hat{\mathbf{P}}_{k-1} \mathbf{h}_k + \frac{R_k}{\beta^2}}. \quad (9)$$

With Eqs. (6) and (9), it is possible to optimize the subsequent encoding  $\mathbf{h}_k$  by

$$\max_{\mathbf{h}_k} \mathcal{L}, \quad \text{s.t. } \mathcal{C}(\mathbf{h}_k) \quad (10)$$

where  $\mathcal{C}(\mathbf{h}_k)$  denotes the practical constraints on the encoding  $\mathbf{H}_k$ . We would like to note that, although derived from an estimation-theoretic perspective, the CRB-based criterion quantifies the same objective of posterior uncertainty reduction as the mutual-information-based formulation. For convenience, this formulation is hereafter referred to as AIME-CRB.

Under this formulation, the design of information-optimal encoding is unified as a constrained optimization problem driven by posterior PDF. Once a specific information criterion and the physical constraints on the encoding are specified, the structure of the optimal encoding follows directly from the solution of this optimization problem. Consequently, the AIME framework itself is not tied to a particular form of information measure or constraint, but provides a general principle for encoding design that can be instantiated under different system configurations.

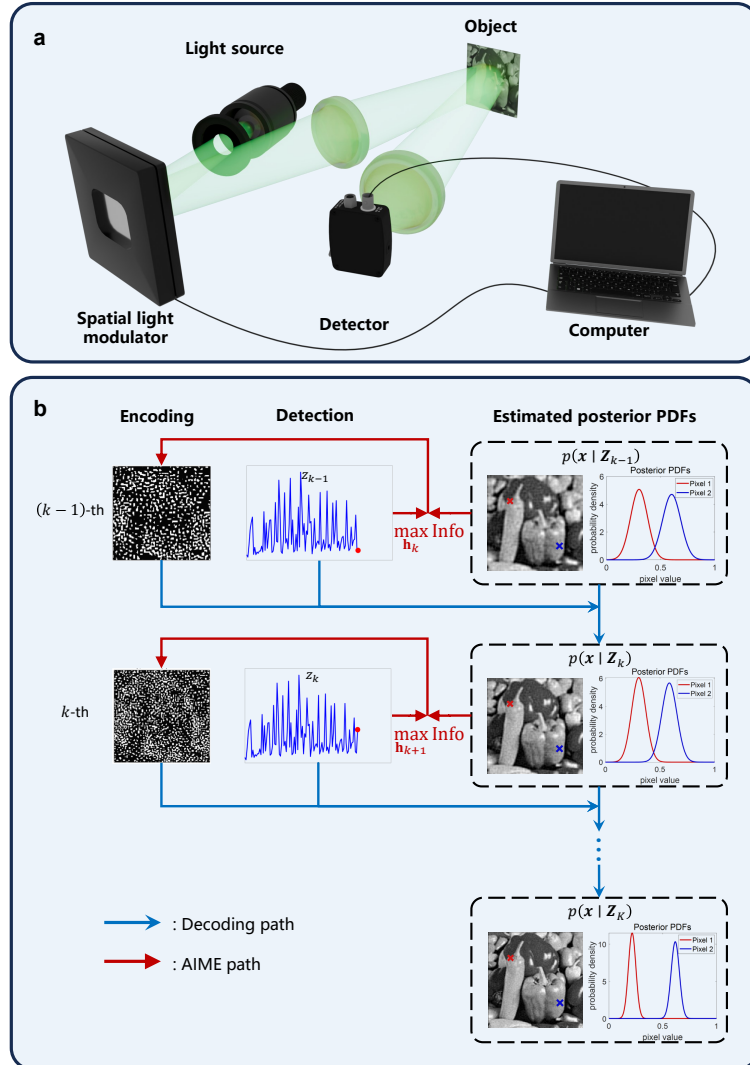


**Fig. 1:** Overview of the proposed framework for adaptive information-maximization encoding (AIME) in GI. The optimal encoding is optimized by maximizing the information of the object to be imaged contained in the detection signal. The information is calculated by the forward detection model and posterior PDFs.

## 2.2 Information-optimal encoding in an ideal energy-constrained regime

Based on the information-theoretic objective derived in the previous subsection, we first examine AIME in an idealized yet physically meaningful encoding regime. Specifically, we consider a total-energy constraint on the encoding light fields, which captures a fundamental limitation in optical imaging systems. This regime serves as a benchmark scenario for revealing the intrinsic structure of information-optimal encoding. Under this constraint, the optimal encoding admits a closed-form analytical solution, as established in the following theorem.

**Theorem 1** (Theoretical solution of information-optimal encoding under a total-energy constraint) *Consider the following optimization problem:*

$$\begin{aligned} & \max_{\mathbf{h}_k} \frac{\mathbf{h}_k^\top \mathbf{P}_{k-1} \mathbf{h}_k}{\mathbf{h}_k^\top \mathbf{x}}, \\ & \text{s.t. } \|\mathbf{h}_k\|_1 = C, \mathbf{h}_k \succeq \mathbf{0}, \end{aligned} \quad (11)$$

where  $\mathbf{P}_{k-1}$  is a positive definite covariance matrix,  $\mathbf{x}$  is a non-negative vector, and  $C > 0$  is a constant. Then the above problem admits an analytical optimal solution. Specifically, the optimal encoding vector is given by

$$\hat{\mathbf{h}}_k = \mathbf{e}_{\hat{i}}, \quad \hat{i} = \arg \max_i \frac{(\mathbf{P}_{k-1})_{ii}}{x_i}, \quad (12)$$

where  $\mathbf{e}_{\hat{i}}$  denotes the standard basis vector whose  $\hat{i}$ -th element is one and all other elements are zero.

This Theorem establishes that, in the ideal energy-constrained regime, information-optimal encoding necessarily reduces to an adaptive point-wise scanning strategy. Importantly, this point-wise structure does not imply a predetermined or fixed scanning order, but instead, varies according to the evolving posterior statistics. For the CRB-based objective shown as Eq. (9), although a closed-form analytical solution of the optimal encoding is difficult to derive, numerical simulations indicate a consistent structural evolution behavior: the optimal encoding initially appears as a diffuse illumination pattern and gradually concentrates into a localized spot as the number of acquired measurements increases. Figure 2 provides an illustrative visualization of the AIME encoding patterns, where panels **a** and **b** correspond to two representative imaging objects. To ensure a fair comparison, the first encoding pattern is identically initialized as the first Hermite–Gaussian mode [39] for all cases. The results visually corroborate the theoretical prediction that information-optimal encoding evolves toward an adaptive point-wise structure under the total-energy constraint, which fundamentally differs from conventional raster-scan imaging in that the scanning order is not fixed but adaptively determined by the statistical structure of the object. A quantitative experimental comparison with conventional full-sampling point-wise scanning under identical total-energy and noise conditions is shown in Fig. 3. Here, AIME consistently achieves higher reconstruction quality than traditional imaging, particularly in low-SNR regimes. In specific, with approximately 50% sampling, AIME yields a

visually recognizable reconstruction at a detection SNR of 8.47 dB, whereas conventional imaging with 100% sampling fails to recover the object reliably. Even when both methods operate at full sampling, AIME produces noticeably improved image quality, with an increase of about 0.2 in SSIM. As the detection SNR further decreases, the object becomes nearly indistinguishable in conventional imaging, while AIME remains capable of providing a coarse yet informative reconstruction. Details of the experimental setting for this comparison is presented in Materials and Methods. These results demonstrate that the adaptive encoding strategy enables more efficient information utilization than fixed raster-scan acquisition in the ideal energy-constrained regime.

An alternative intuition for the emergence of point-wise optimal encoding can be drawn from CS. It is well established in CS theory that sparse signals can be efficiently acquired through incoherent measurements in a conjugate domain, for example, spatially sparse signals can be recovered from partial Fourier measurements [40]. In the present imaging scenario, natural scenes are often sparse in transform domains such as the DCT domain. From this perspective, concentrating measurements on a limited set of spatial locations can be viewed as an intuitive counterpart to selectively probing sparse degrees of freedom in a conjugate domain, offering a qualitative analogy to the point-wise scanning behavior predicted by the information-theoretic analysis.

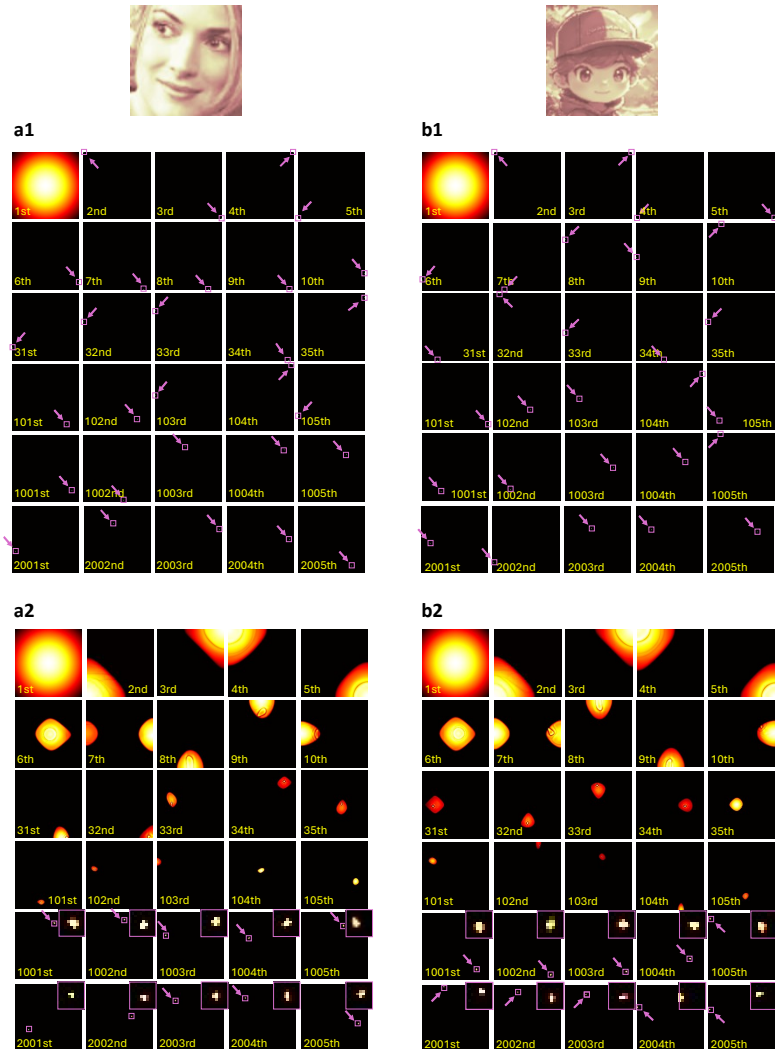


**Fig. 2:** Illustration of the theoretical result of AIME patterns, each pattern is normalized to its maximum value for visualization. Figures **a1**, **a2** and **b1**, **b2** show the AIME results of two different imaging objects. **a1** and **b1** are patterns obtained by analytical solution of Eq. (12), each of which show exactly a scanning point; and the position of the point is marked with a purple arrow and box. **a2** and **b2** are patterns obtained by minimizing the mean CRB, which gradually become a small-size spot as the number of measurements increases; and the spot region in each pattern is displayed in an enlarged view. The first Hermite-Gaussian pattern is employed as the first frame of encoding pattern here.

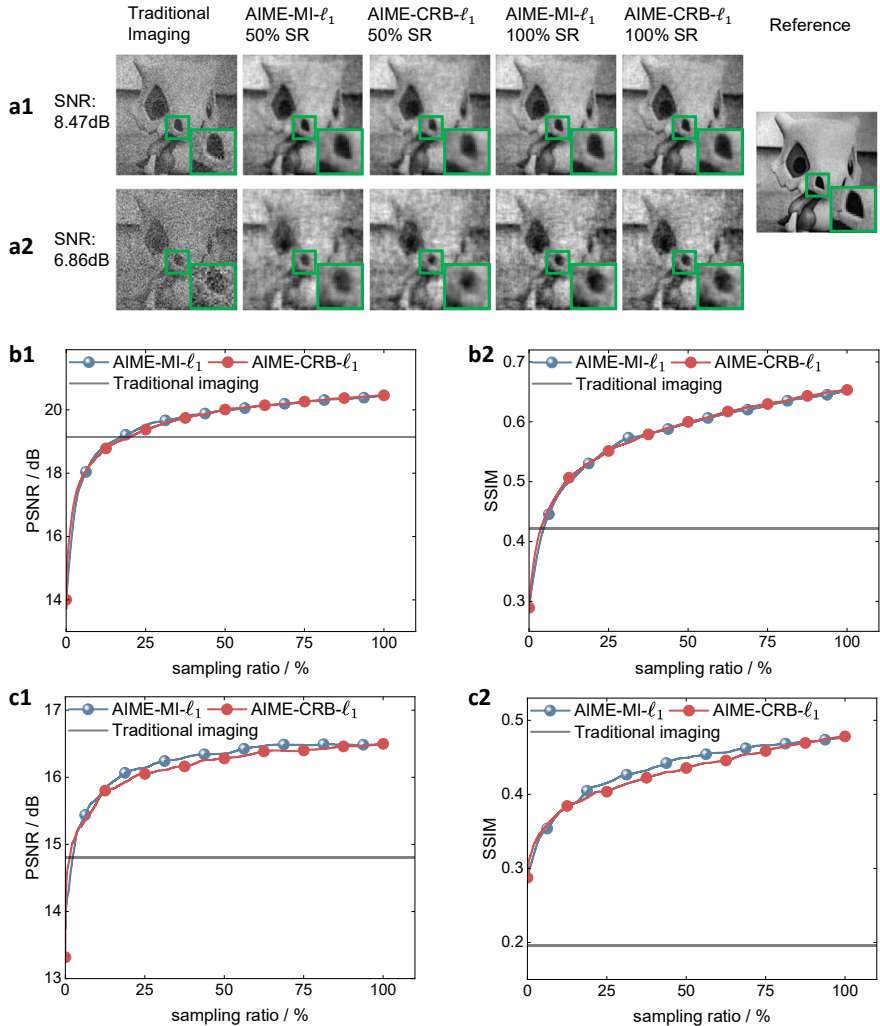


**Fig. 3:** Experimental comparison of imaging results of AIME and traditional imaging. **a:** Representative reconstructed images obtained by traditional imaging and AIME under sampling ratios (SRs) of 50% and 100%. Results are shown for two signal-to-noise ratio (SNR) levels, as indicated on the left. The reference image is shown on the right, which is obtained by full-sampling point-wise scanning under a significantly high SNR. **b:** Quantitative evaluation of imaging quality in terms of PSNR and SSIM as functions of the sampling ratio for the case of  $\text{SNR} = 8.74 \text{ dB}$ . The horizontal gray lines indicate the performance of traditional full-sampling (100% SR) imaging for reference. **c:** Corresponding PSNR and SSIM curves for the case of  $\text{SNR} = 6.86 \text{ dB}$ .

### 2.3 Information-optimal encoding under realistic modulation constraints

The preceding analysis establishes the intrinsic structure of information-optimal encoding under an idealized total-energy constraint. In practical GI systems, however, additional modulation constraints on the encoding patterns are inevitably imposed. It is therefore essential to examine whether the advantages of AIME persist under such realistic conditions. To this end, beyond the ideal total-energy constraint, we further impose a bounded-amplitude constraint on the encoding patterns,

$$0 \leq h_{k,i} \leq C, \quad \forall i, \quad (13)$$

which reflects realistic hardware limitations such as the finite modulation depth of spatial light modulators or digital micromirror devices.

Under such constraints, the closed-form analytical solution derived above no longer applies, and the information-optimal encoding is therefore obtained numerically by solving the resulting constrained optimization problem. Figure 4 provides an illustrative visualization of the joint evolution of the reconstructed image and the optimized encoding patterns under the proposed strategy. Two different imaging scenes, namely *cameraman* and *pepper*, are considered, and the peak signal-to-noise ratio (PSNR) is used to quantify the imaging quality. Figures 4(a1) and (b1) show the reconstructed images together with the corresponding optimized encoding patterns at different sampling ratios (SRs), where the selected SRs correspond to the marked points in Figs. 4(a2) and (b2), respectively. The optimized encoding patterns exhibit a clear coarse-to-fine evolution as the SR increases. At low SRs, the patterns consist of large-scale speckle-like structures, whereas at higher SRs, finer spatial features gradually emerge. This behavior is consistent with the gradual refinement of the posterior distribution in the Bayesian filtering process, where early measurements focus on coarse information content and subsequent measurements concentrate on increasingly localized spatial details. The corresponding PSNR curves shown in Figs. 4 (a2) and (b2) demonstrate a rapid improvement in reconstruction quality at the early stage of sampling, indicating the high information efficiency of the proposed strategy under limited measurements. To further illustrate the accuracy and uncertainty evolution of the reconstruction, the posterior probability density functions (PDFs) of two representative pixel locations (marked by red and blue crosses in the reconstructed images) are plotted in Figs. 4 (a3) and (b3). As SR increases, the posterior PDFs become progressively sharper, reflecting the systematic reduction of estimation uncertainty and the convergence of pixel-wise intensity estimates. By comparing the results obtained for different imaging scenes, it is evident that the optimized encoding patterns are also strongly scene-dependent under the bounded-amplitude constraint. This observation is fully consistent with the theoretical formulation of AIME and highlights its ability to adaptively allocate measurements according to the estimated statistical state of the imaging object.

We further compare the proposed AIME strategy with several existing encoding patterns in GI, including pseudo-thermal random patterns, Walsh–Hadamard patterns, and Hermite–Gaussian patterns [39]. For all encoding strategies, the same

Bayesian filtering framework is employed for image estimation to ensure a fair comparison. Figure 5 summarizes the imaging results for three representative scenes acquired under different sampling ratios (SRs) and signal-to-noise ratios (SNRs) (Fig. 5 a1–a3). For all tested scenes, both AIME-based strategies consistently yield superior reconstruction quality compared with other encoding patterns, as evidenced by clearer structural details and significantly reduced noise artifacts. The corresponding PSNR and SSIM values are reported under each reconstructed image, where AIME achieves the highest quantitative performance across all cases. The evolution of PSNR and SSIM as functions of the sampling ratio is further plotted in Figs. 5 b1–b3 and c1–c3, respectively. These results reveal that AIME exhibits a pronounced advantage at early measurement stages, where substantial image quality improvements are already achieved at low sampling ratios. As the number of measurements increases, AIME continues to provide steady performance gains, whereas the imaging quality obtained with other encoding patterns rapidly saturates. This behavior demonstrates the strong compressed-sampling capability of AIME and its effectiveness in allocating measurements to the most informative degrees of freedom.

To further quantify the information acquisition capability of different encoding strategies, we explicitly compute the cumulative mutual information and Fisher information accumulated in the detection signals. Specifically, the cumulative mutual information is calculated as  $\sum_k \frac{1}{2} \ln \left( 1 + \frac{\mathbf{H}_k \hat{\mathbf{P}}_{k-1} \mathbf{H}_k^\top}{R_k} \right)$ , while the cumulative Fisher information is evaluated by  $\text{Tr}(\hat{\mathbf{P}}_k^{-1})$ . The corresponding results is shown in Fig. 5 d1–d3, closely follow the trends observed in the image quality metrics. Across different SRs and noise levels, AIME consistently enables the detection signals to acquire substantially more information about the imaging object than other comparison encoding schemes. This strong agreement between information-theoretic measures and reconstruction quality confirms that the superior imaging performance of AIME is a direct consequence of its enhanced information acquisition capability, rather than heuristic effects.

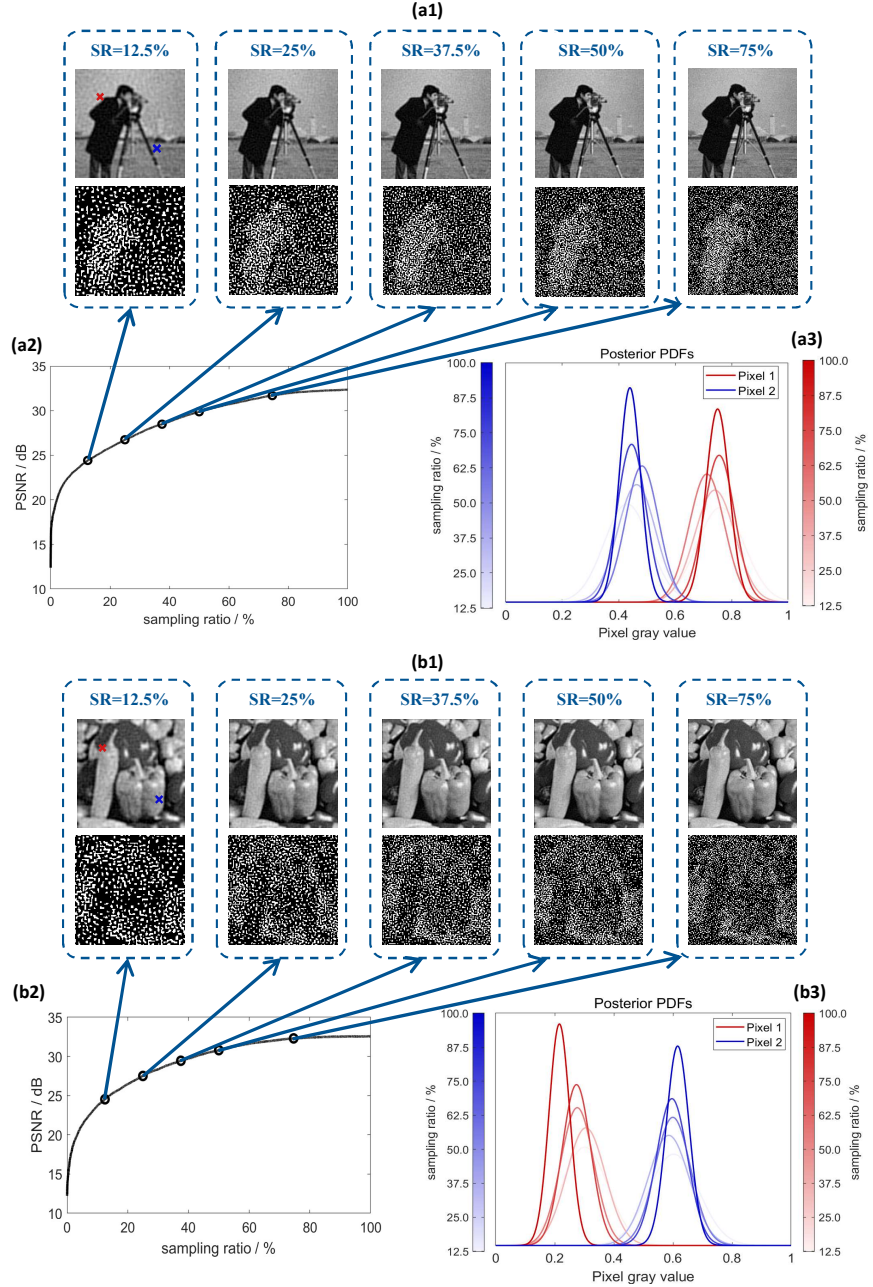


**Fig. 4:** Simulation results for illustrating the evolution process of the proposed strategy on two different imaging scenes. (a1) and (b1) show the evolution of estimated images and corresponding optimized encoding patterns with sampling ratio increasing for two imaging scenes, respectively; (a2) and (b2) show evolution of PSNR indicators with the increase in sampling; (a3) and (b3) show evolution of estimated PDFs of two selected pixels marked on each, respectively.

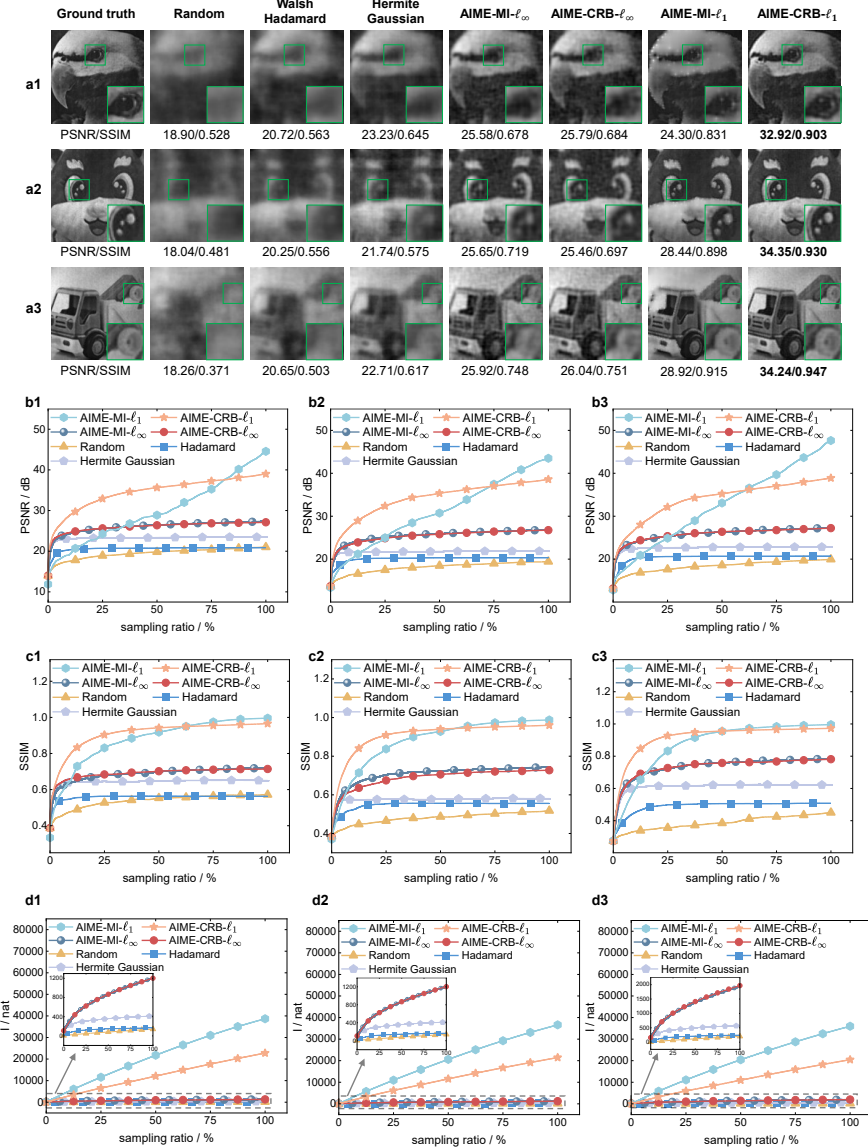


**Fig. 5:** Experimental imaging results for comparison between AIME and some typical encoding patterns, **a1**, **a2**, and **a3** show three different representative cases. For AIME, encoding strategies under both total-energy and amplitude constraints are evaluated, and shown with suffix ‘- $\ell_1$ ’ and ‘-ell<sub>infinity</sub>’, respectively. The SR and SNR for these simulations are: **a1** SNR around 18 dB, and 25 % SR; **a2** SNR around 18.5 dB, and 37.5 % SR; **a3** SNR around 20 dB, and 37.5 % SR. Corresponding PSNR and SSIM indicators of imaging results as SR increases are shown in **b1**, **b2**, and **b3**, respectively.

### 3 Discussion

In this work, an adaptive information-maximization encoding strategy is developed for ghost imaging (GI). The proposed framework is intended to serve as a generally applicable approach for information-optimal encoding in computational imaging systems with the encoding-decoding mode, provided that the forward imaging model can be explicitly characterized. In the present study, the forward model is formulated as a simplified linear model and demonstrated using a spatial-domain GI system with sequential bucket detection. In practical imaging scenarios, however, the forward process may be considerably more complex. Forward modeling of GI under realistic conditions, including effects such as optical blurring, down-sampling, and noise, has been extensively investigated in the literature [41–43]. Moreover, since Bayesian filtering theory is not restricted to linear systems, the proposed strategy can, in principle, be generalized to computational imaging problems governed by nonlinear forward models, such as phase retrieval and coherent detection. Beyond the form of the forward model, the framework is also not restricted to a specific sensing configuration. Although AIME is demonstrated with sequential bucket detection, the underlying Bayesian filtering and information optimization principles can be naturally extended to batch-measurement settings, which corresponds to computational imaging systems using two-dimensional sensor arrays. In such cases, multiple measurements are acquired simultaneously, and the framework can be generalized to adaptive or semi-adaptive encoding design in a higher-dimensional measurement space, suggesting its applicability to a broader class of computational imaging systems, like GI camera [44].

In addition to the forward model, another essential component of the proposed framework is the setting of the initial image PDF. In the presented study, a general prior is adopted by imposing constraints in the image frequency domain, which allows an PDF to be defined for an entirely unknown imaging scene. While this choice provides a concise and robust prior for Bayesian filtering, it can be further improved by incorporating alternative analytical image prior that better capture higher-order statistical properties of natural images [45]. Furthermore, with the development of deep neural models, image priors can now be effectively learned from data using deep generative models. In scenarios where a sufficiently large and representative training dataset is available, the proposed strategy can be naturally combined with image priors provided by trained generative models [46, 47]. Such learned priors are expected to offer a more expressive statistical representation than the general analytical prior employed in this work, potentially leading to further performance improvements.

Altogether, this work highlights the potential of information-theoretic encoding design as a principled approach to GI and, more broadly, to computational imaging systems. By explicitly modeling the information carried by detection signals under realistic physical constraints imposed by the imaging system, the proposed framework provides a systematic methodology to characterize and approach fundamental imaging limits. The finding that point-like encoding emerges as information-optimal under a total-energy constraint further offers a new information-theoretic perspective on the widespread use of point-to-point sampling strategies in biological vision systems. This result suggests that such sampling schemes may reflect an underlying principle of efficient information acquisition rather than merely engineering convenience. Beyond GI,

the proposed framework is expected to inspire further information-theoretic studies on the evaluation and optimization of imaging and sensing systems, with potential implications for a broad range of applications, including autonomous sensing, machine vision, and data-efficient perception tasks. Importantly, in numerous such systems, flexible light-field modulation platforms such as metasurfaces and programmable photonic devices are increasingly employed as core encoding components, which imposes structured physical constraints on the encoding space. Incorporating those constraints into the proposed framework is supposed to offer a principled pathway that integrates emerging hardware platforms with the information-optimal encoding design.

## Materials and Methods

### Details for encoding optimization

The optimization of the objective function is formulated as a constrained problem and solved using Projected Gradient Descent (PGD), which alternates between gradient descent and projection of parameters onto the constraint domain. Specifically, during the gradient descent step, we employ the SGD optimizer with learning rates of  $1 \times 10^9$  and  $1 \times 10^5$  for the mutual information and CRLB objective function, respectively. All other hyperparameters are set to the default values in PyTorch. To balance computational efficiency and estimation quality, we perform 100 PGD iterations per encoding optimization. All simulations are implemented in PyTorch 2.5.1 with CUDA 12.1 and executed on an NVIDIA GeForce RTX 3090 GPU. One epoch comprising both Bayesian filtering and encoding optimization takes approximately 0.2 s for a  $128 \times 128$  image.

### Measurement of parameters $\beta$ and $R_k$ in the experiment

In the experiment, to determine the forward model shown as Eq. (1), the factor  $\beta$  and the noise level  $\{R_k\}$  are pre-measured. Specifically, a whiteboard with uniform reflectance is used as the imaging object for estimating  $\beta$  and several Hadamard encoding patterns  $\mathbf{h}^{(1)}, \dots, \mathbf{h}^{(M)}$  are pre-set. Then, the object is repetitively illuminated  $L$  times with each pattern, and detection light intensity signals  $\mathbf{z}^{(1)}, \dots, \mathbf{z}^{(M)}$  are recorded, where each  $\mathbf{z}^{(m)} \in \mathcal{R}^L$ . And  $\beta$  is estimated by

$$\beta = \left\langle \frac{\bar{z}^{(m)}}{\sum_i \mathbf{h}_i^{(m)}} \right\rangle_m$$

where  $\bar{z}^{(m)}$  denotes the average on elements of  $\mathbf{z}^{(m)}$  and  $\langle \cdot \rangle_m$  denotes the average on those estimation results of  $\beta$  with  $m = 1, \dots, M$  patterns.

For noise calibration of  $R_k$ , the detection noise variance, denoted as  $\sigma_{(m)}^2$  corresponding to the  $m$ -th Hadamard pattern, is estimated using the sample variance over  $L$  measurements:

$$\sigma_{(m)}^2 = \frac{\sum_{l=1}^L (z_l^{(m)} - \bar{z}^{(m)})^2}{L - 1}, \quad (14)$$

where  $z_l^{(m)}$  represents the  $l$ -th measurement of the  $m$ -th pattern, and  $\bar{z}^{(m)}$  is the sample mean. Consequently, the average signal-to-noise ratio (SNR) is defined as:

$$\text{SNR} = 10 \log_{10} \left( \frac{\langle \bar{z}^{(m)} \rangle_m}{\langle \sigma_{(m)}^2 \rangle_m} \right). \quad (15)$$

The illumination intensity of the light source is adjusted to ensure the experimental SNR matches the target value. Given that the detection noise is modeled as  $w^2 \mathbf{Hx}$ , the noise parameter  $w^2$  for each pattern can be estimated via  $w^{2(m)} = \sigma_{(m)}^2 / \bar{z}^{(m)}$ . The ensemble average is denoted as  $\langle w^{2(m)} \rangle_m$ .

In the numerical process, the acquired bucket detection values are normalized by a factor  $\beta$ . Therefore, the effective noise parameter used in the computation is scaled accordingly:

$$w_{\text{eff}}^2 = \frac{\langle w^{2(m)} \rangle_m}{\beta^2}. \quad (16)$$

By varying the light intensity and repeating the aforementioned procedure,  $w^2$  values corresponding to different detection intensity ranges are recorded. This parameter is essential for pattern optimization based on the Cramér-Rao Bound (CRB). In this work, we employ the same  $w^2$  value as utilized in the mutual information-based optimization framework.

## Experimental setting in comparison with traditional imaging

In comparative experiments involving full-sampling conventional imaging under low SNR conditions, the dominant source of noise is set to arise from background light introduced with another LED source. Consequently, the background noise, denoted as  $\sigma_{\text{back}}^2$ , is modeled as additive Gaussian noise with constant variance. To quantify the SNR,  $L$  measurements are acquired using a completely dark pattern. Let  $z_{\text{back}}^{(l)}$  represent the signal intensity of the  $l$ -th measurement, and  $\bar{z}_{\text{back}}$  denote the average intensity. The background noise variance  $\sigma_{\text{back}}^2$  and the experimental SNR are estimated as follows:

$$\sigma_{\text{back}}^2 = \frac{\sum_{l=1}^L (z_{\text{back}}^{(l)} - \bar{z}_{\text{back}})^2}{L - 1}, \quad (17)$$

$$\text{SNR} = 10 \log_{10} \left( \frac{\bar{z}_{\text{back}}}{\sigma_{\text{back}}} \right). \quad (18)$$

## Setting the initial image PDF

In the proposed strategy, an initial Gaussian PDF  $p(\mathbf{x}) = \mathcal{N}(\mathbf{x}_0, \mathbf{P}_0)$  of the object's image is set. To specify the parameters  $\mathbf{x}_0$  and  $\mathbf{P}_0$ , we adopt a commonly used statistical model for natural images, in which the frequency-domain coefficients  $\{a(\mathbf{f})\}$  of

images [48] follow a Laplacian distribution

$$p(a(\mathbf{f})) = \frac{1}{2b(\mathbf{f})} \exp \left[ -\frac{|a(\mathbf{f}) - \mu(\mathbf{f})|}{b(\mathbf{f})} \right], \quad (19)$$

where  $\mu(\mathbf{f}) = 0$  for those non-zero-frequency components,  $b(\mathbf{f}) \propto (|\mathbf{f}|)^{-\gamma}$  with  $\gamma \in [1, 1.2]$ . Based on Eq. (19), the parameters of the initial Gaussian PDF are set as

$$\mathbf{x}_0 = \mathbf{0} \quad (20a)$$

$$\mathbf{P}_0 = \Psi^\top 2\mathbf{b}\mathbf{b}^\top \Psi \quad (20b)$$

where  $\mathbf{b} = [b(\mathbf{f}_0), b(\mathbf{f}_1), \dots]^\top$  and  $\Psi$  denotes the digital cosine transform (DCT) matrix. It should be noted that, owing to the high dimensionality of image signals and the central limit theorem, although the frequency-domain coefficients are modeled as independent Laplacian variables, the image-domain pixels, being weighted superpositions of a large number of such coefficients, can be well approximated as following a Gaussian distribution.

## Supplementary information

Materials include the Supplementary Text, Figs. S1 to S10, and Reference [1].

## Data availability

Data are available from the corresponding author on request.

## Funding

This work is supported by the National Natural Science Foundation of China (62201165, 62475270) and the National Key Research and Development Program of China (2024YFF0505601).

## Author contributions

C. Hu and S. Han conceived the idea and supervised the study. J. Sun and C. Hu performed most of the theoretical derivation. J. Sun and C. Hu conducted the experiment under discussion with Z. Bo, Z. Liu and M. Chen. L. Du and W. Liu provided the initial simulation codes for Bayesian filtering of GI, and contribute to code modification. J. Sun and C. Hu analyzed the experimental data, and wrote the original draft. All authors discussed the results contributed to editing and revising the paper.

## Competing interests

The authors declare no competing interests.

## Appendix A Theoretical derivation of the objective function for AIME-MI and AIME-CRB

In the proposed strategy, the mutual information  $I(z_k, \mathbf{x} \mid \mathbf{Z}_{k-1})$  is specifically calculated as follows

$$\begin{aligned}
I(z_k, \mathbf{x} \mid \mathbf{Z}_{k-1}) &= H(\mathbf{x} \mid \mathbf{Z}_{k-1}) - H(\mathbf{x} \mid \mathbf{Z}_k) \\
&= \left[ \frac{N}{2} (1 + \log 2\pi) + \frac{1}{2} \log |\widehat{\mathbf{P}}_{k-1}| \right] - \left[ \frac{N}{2} (1 + \log 2\pi) + \frac{1}{2} \log |\widehat{\mathbf{P}}_k| \right] \\
&= \frac{1}{2} \log \frac{|\widehat{\mathbf{P}}_{k-1}|}{|\widehat{\mathbf{P}}_k|} = \frac{1}{2} \log \frac{|\widehat{\mathbf{P}}_{k-1}|}{|(\mathbf{I} - \beta \mathbf{K}_k \mathbf{h}_k^\top) \widehat{\mathbf{P}}_{k-1}|} \\
&= \frac{1}{2} \log \frac{1}{|\mathbf{I} - \beta \mathbf{K}_k \mathbf{h}_k^\top|}.
\end{aligned} \tag{A1}$$

where  $H(\cdot)$  is the information entropy, which can be expressed as  $\frac{1}{2} \log (2\pi e)^N \det \sum$  for a  $N$ -variable Gaussian distribution,  $\sum$  is the covariance matrix of the corresponding variables, and  $|\mathbf{P}|$  denotes the determinant of matrix  $\mathbf{P}$ . By using the property of matrix determinant  $|\mathbf{I} + \mathbf{u}\mathbf{v}^\top| = 1 + \mathbf{u}^\top \mathbf{v}$ , the above expression can be further simplified

$$\begin{aligned}
I(z_k, \mathbf{x} \mid \mathbf{Z}_{k-1}) &= \frac{1}{2} \log \frac{1}{1 - \beta \mathbf{K}_k^\top \mathbf{h}_k} \\
&= \frac{1}{2} \log \frac{1}{1 - \left( \beta^2 \mathbf{h}_k \widehat{\mathbf{P}}_{k-1} \mathbf{h}_k^\top + R_k \right)^{-1} \beta^2 \mathbf{h}_k \widehat{\mathbf{P}}_{k-1} \mathbf{h}_k} \\
&= \frac{1}{2} \log \frac{1}{1 - \frac{\beta^2 \mathbf{h}_k \widehat{\mathbf{P}}_{k-1} \mathbf{h}_k^\top}{\beta^2 \mathbf{h}_k \widehat{\mathbf{P}}_{k-1} \mathbf{h}_k^\top + R_k}} \\
&= \frac{1}{2} \log \frac{\beta^2 \mathbf{h}_k \widehat{\mathbf{P}}_{k-1} \mathbf{h}_k^\top + R_k}{R_k}
\end{aligned} \tag{A2}$$

The mean CRB is calculated as follows

$$\begin{aligned}
\text{mCRB} &= \text{Tr}(\widehat{\mathbf{P}}_k) \\
&= \text{Tr} \left( (\mathbf{I} - \beta \mathbf{K}_k \mathbf{h}_k^\top) \widehat{\mathbf{P}}_{k-1} \right) \\
&= \text{Tr} \left( \widehat{\mathbf{P}}_{k-1} \right) - \text{Tr} \left( \beta \mathbf{K}_k \mathbf{h}_k^\top \widehat{\mathbf{P}}_{k-1} \right) \\
&= \text{Tr} \left( \widehat{\mathbf{P}}_{k-1} \right) - \text{Tr} \left( \beta^2 \widehat{\mathbf{P}}_{k-1} \mathbf{h}_k \left( \beta^2 \mathbf{h}_k^\top \widehat{\mathbf{P}}_{k-1} \mathbf{h}_k + R_k \right)^{-1} \mathbf{h}_k^\top \widehat{\mathbf{P}}_{k-1} \right)
\end{aligned} \tag{A3}$$

where  $\text{Tr}(\mathbf{P})$  denotes the trace of matrix  $\mathbf{P}$ . By using the property of matrix trace, the above expression can be rewritten as

$$\begin{aligned} \text{mCRB} &= \text{Tr} \left( \widehat{\mathbf{P}}_{k-1} \right) - \beta^2 \text{Tr} \left( \mathbf{h}_k^\top \widehat{\mathbf{P}}_{k-1}^2 \mathbf{h}_k \left( \beta^2 \mathbf{h}_k^\top \widehat{\mathbf{P}}_{k-1} \mathbf{h}_k + R_k \right)^{-1} \right) \\ &= \text{Tr} \left( \widehat{\mathbf{P}}_{k-1} \right) - \text{Tr} \left( \frac{\mathbf{h}_k^\top \widehat{\mathbf{P}}_{k-1}^2 \mathbf{h}_k}{\mathbf{h}_k^\top \widehat{\mathbf{P}}_{k-1} \mathbf{h}_k + \frac{R_k}{\beta^2}} \right) \\ &= \text{Tr} \left( \widehat{\mathbf{P}}_{k-1} \right) - \frac{\mathbf{h}_k^\top \widehat{\mathbf{P}}_{k-1}^2 \mathbf{h}_k}{\mathbf{h}_k^\top \widehat{\mathbf{P}}_{k-1} \mathbf{h}_k + \frac{R_k}{\beta^2}} \end{aligned} \quad (\text{A4})$$

## Appendix B Proof of Theorem 1

Here we give the proof of Theorem 1 in the article, which indicates that the optimal encoding pattern of AIME-MI under the total-energy constraint correspond to a scanning point.

**Theorem 2** (Theoretical solution of AIME-MI under the total-energy constraint) *Consider the following optimization problem:*

$$\begin{aligned} &\max_{\mathbf{h}_k} \frac{\mathbf{h}_k^\top \mathbf{P}_{k-1} \mathbf{h}_k}{\mathbf{h}_k^\top \mathbf{x}}, \\ &\text{s.t. } \|\mathbf{h}_k\|_1 = C, \mathbf{h}_k \succeq \mathbf{0}, \end{aligned} \quad (\text{B5})$$

where  $\mathbf{P}_{k-1}$  is a positive definite covariance matrix,  $\mathbf{x}$  is a non-negative vector, and  $C > 0$  is a constant. Then the above problem admits an analytical optimal solution. Specifically, the optimal encoding vector is given by

$$\hat{\mathbf{h}}_k = \mathbf{e}_{\hat{i}}, \quad \hat{i} = \arg \max_i \frac{(\mathbf{P}_{k-1})_{ii}}{x_i}, \quad (\text{B6})$$

where  $\mathbf{e}_{\hat{i}}$  denotes the standard basis vector whose  $\hat{i}$ -th element is one and all other elements are zero.

*Proof of Theorem 2* We first note that the objective function is a ratio of two positive homogeneous functions of  $\mathbf{h}_k$ . Following standard results in fractional programming [49], maximizing the ratio

$$\frac{\mathbf{h}_k^\top \mathbf{P}_{k-1} \mathbf{h}_k}{\mathbf{h}_k^\top \mathbf{x}}, \quad (\text{B7})$$

is equivalent to finding the largest scalar  $\alpha$  such that

$$\mathbf{h}_k^\top \mathbf{P}_{k-1} \mathbf{h}_k - \alpha \mathbf{h}_k^\top \mathbf{x} \geq 0 \quad (\text{B8})$$

admits a feasible solution of  $\mathbf{h}_k$  under the same constraints. This lead to an equivalent parametric optimization problem as

$$\max_{\mathbf{h}_k} \left( \mathbf{h}_k^\top \mathbf{P}_{k-1} \mathbf{h}_k - \alpha \mathbf{h}_k^\top \mathbf{x} \right), \quad \text{s.t. } \|\mathbf{h}_k\|_1 = C, \mathbf{h}_k \succeq \mathbf{0}, \quad (\text{B9})$$

where

$$\alpha = \max_{\mathbf{h}_k} \frac{\mathbf{h}_k^\top \mathbf{P}_{k-1} \mathbf{h}_k}{\mathbf{h}_k^\top \mathbf{x}}. \quad (\text{B10})$$

This can be further rewritten to a standard quadratic form

$$\mathbf{h}_k^\top \mathbf{P}_{k-1} \mathbf{h}_k - \alpha \mathbf{h}_k^\top \mathbf{x} = \left( \mathbf{h}_k - \frac{\alpha}{2} \mathbf{P}_{k-1}^{-1} \mathbf{x} \right)^\top \mathbf{P}_{k-1} \left( \mathbf{h}_k - \frac{\alpha}{2} \mathbf{P}_{k-1}^{-1} \mathbf{x} \right) - \frac{\alpha^2}{4} \mathbf{x}^\top \mathbf{P}_{k-1}^{-1} \mathbf{x}. \quad (\text{B11})$$

Since  $\mathbf{P}_{k-1}$  is positive definite, the objective is convex with respect to  $\mathbf{h}_k$ . Under the constraints  $\|\mathbf{h}_k\|_1 = C$ , and  $\mathbf{h}_k \succeq \mathbf{0}$ , the feasible region is a simplex, making the extreme points correspond to scaled standard basis vectors  $\{C\mathbf{e}_i\}$ . Therefore, the maximum of the objective function shown as Eq. (B11) is attained at one of the extreme points, implying that the optimal solution  $\hat{\mathbf{h}}_k$  correspond to a standard basis vector.

Substituting  $\mathbf{h}_k = \mathbf{e}_i$  into the original objective yields

$$\frac{\mathbf{h}_k^\top \mathbf{P}_{k-1} \mathbf{h}_k}{\mathbf{h}_k^\top \mathbf{x}} = \frac{\mathbf{e}_i^\top \mathbf{P}_{k-1} \mathbf{e}_i}{\mathbf{e}_i^\top \mathbf{x}} = \frac{(\mathbf{P}_{k-1})_{ii}}{x_i}. \quad (\text{B12})$$

From this, the optimal index  $\hat{i}$  can be obtained by

$$\hat{i} = \arg \max_i \frac{(\mathbf{P}_{k-1})_{ii}}{x_i}, \quad (\text{B13})$$

which leads to the optimal  $\hat{\mathbf{h}}_k = \mathbf{e}_{\hat{i}}$  and complete the proof.  $\square$

## Appendix C Definition of the detection signal-to-noise ratio

Here we would like to discuss about the definition of the detection SNR in GI systems. Typically, the detection SNR in an imaging system is defined as

$$\text{SNR} = 10 \log_{10} \left( \frac{\bar{z}}{\sigma} \right), \quad (\text{C14})$$

where  $\bar{z}$  represents the average value of the detection signal and  $\sigma$  denotes the noise level. In the field of GI, there also exist some other kinds of definitions. For example, the bucket detection SNR (BSNR) is calculated as

$$\text{BSNR} = 10 \log_{10} \left( \frac{\bar{z}^2 - \bar{z}^2}{\sigma} \right), \quad (\text{C15})$$

to measure the level of signal fluctuations. However, this definition only apply to GI systems with randomly fluctuating light fields, and it is not directly related to the detection process. In the field of signal processing, the SNR is defined as

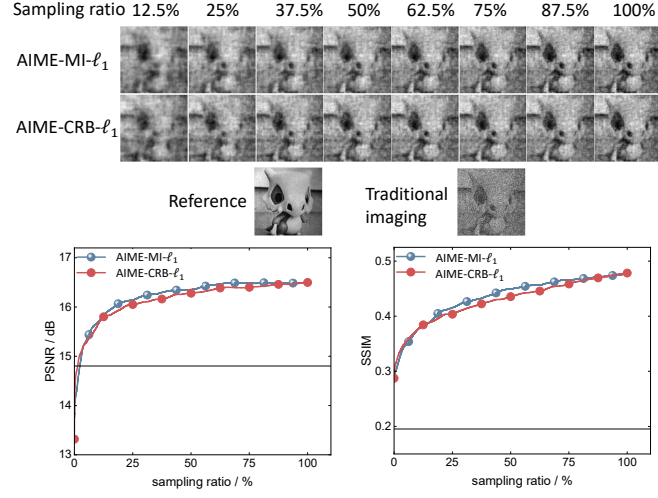
$$\text{SNR} = 10 \log_{10} \left( \frac{P_s}{P_n} \right) = 10 \log_{10} \left( \frac{|z|^2}{|n|^2} \right), \quad (\text{C16})$$

where  $P_s$  denotes the signal power and  $P_n$  is the noise power. Different from traditional signal processing which deal with electronic signals, in GI the signal is in fact an optical

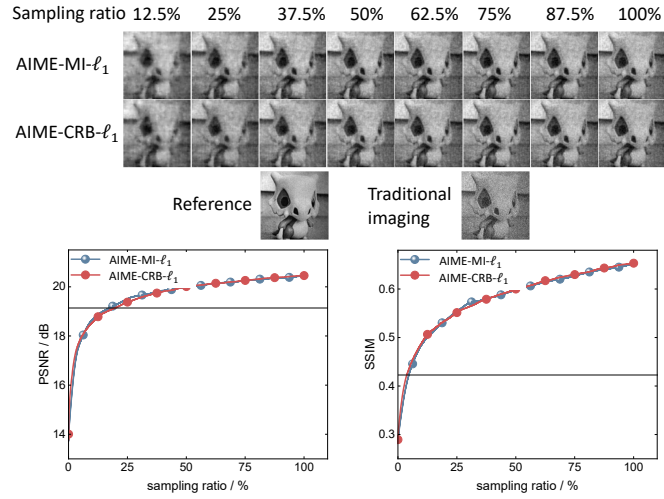
one. Since the detector directly measures the intensity of light fields, the recorded intensity signal can already be considered as the power. Hence, in this study we still use the definition as Eq. (C14).

## Appendix D Detailed comparison results between GI with AIME- $\ell_1$ and fixed point-to-point conventional imaging under different detection SNRs

Figures A1 to A4 show experimental results of four representative imaging scenes for comparing GI with AIME- $\ell_1$  and fixed point-to-point conventional imaging.

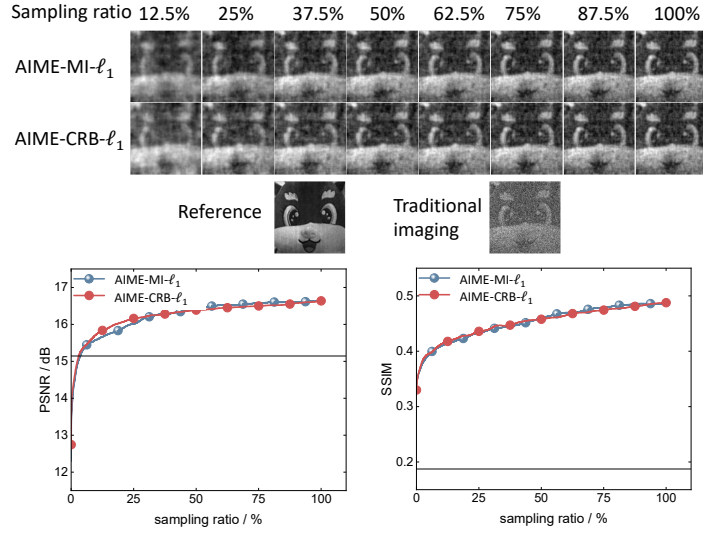


(a) SNR about 6.86dB

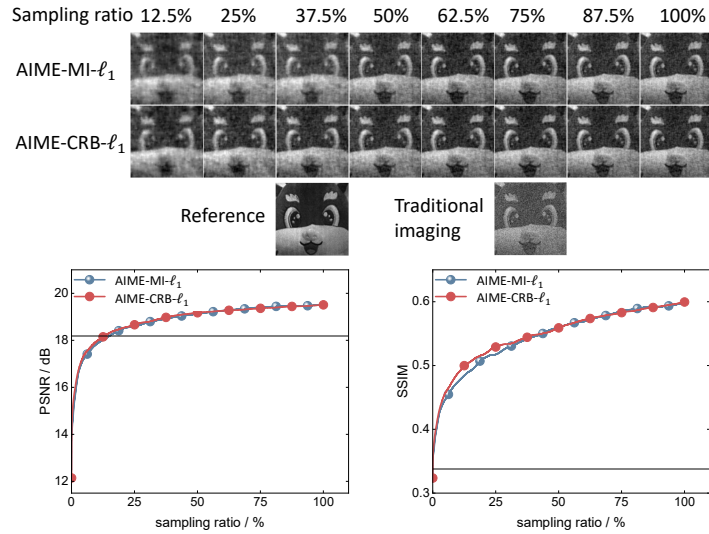


(b) SNR about 8.47dB

**Fig. A1:** Comparison results of scene 1 under different sampling ratios and SNRs, including imaging results and imaging quality

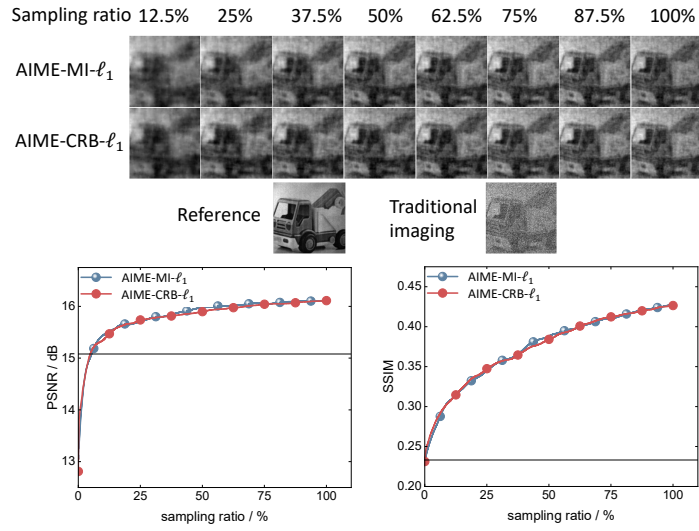


(a) SNR about 5.16dB

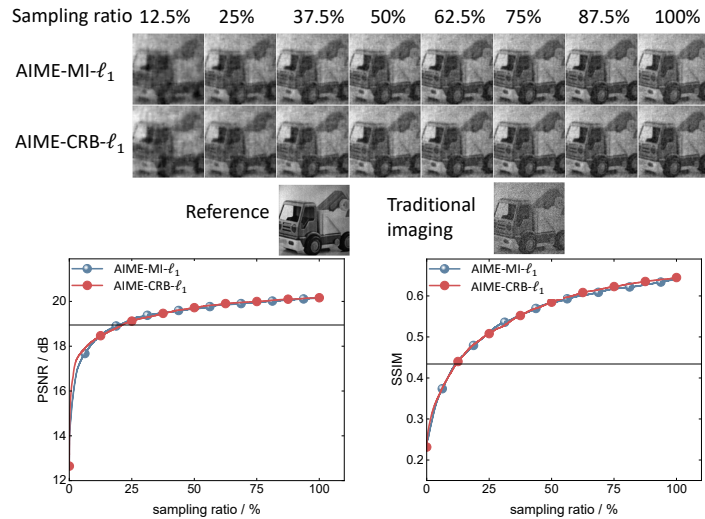


(b) SNR about 7.63dB

**Fig. A2:** Comparison results of scene 2 under different sampling ratios and SNRs, including imaging results and imaging quality

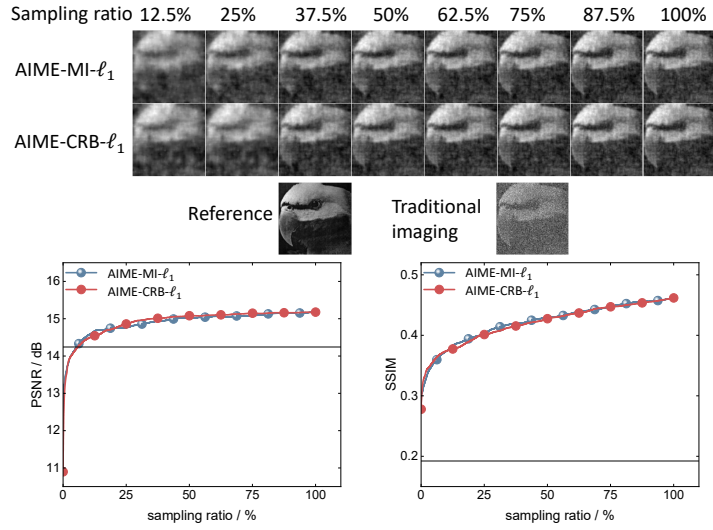


(a) SNR about 5.90dB

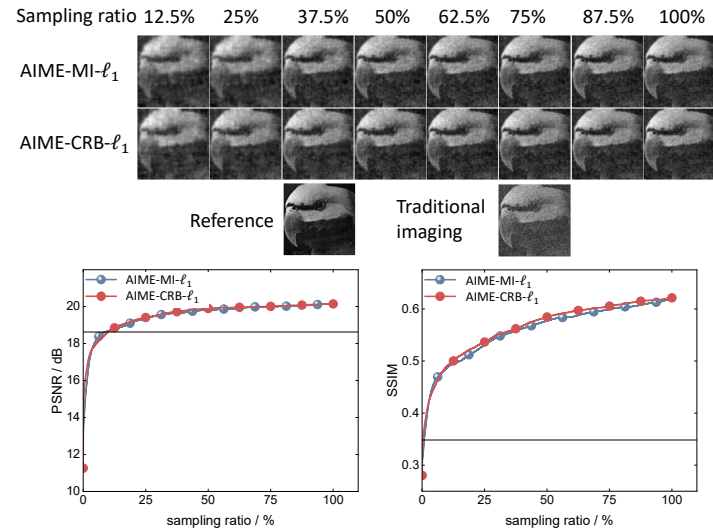


(b) SNR about 7.63dB

**Fig. A3:** Comparison results of scene 3 under different sampling ratios and SNRs, including imaging results and imaging quality



(a) SNR about 3.20dB



(b) SNR about 6.33dB

**Fig. A4:** Comparison results of scene 4 under different sampling ratios and SNRs, including imaging results and imaging quality

## Appendix E Detailed comparison between GI with AIME and existing encoding patterns

Figures A5 to A8 show experimental results of four representative imaging scenes for comparing GI with AIME and existing encoding patterns.

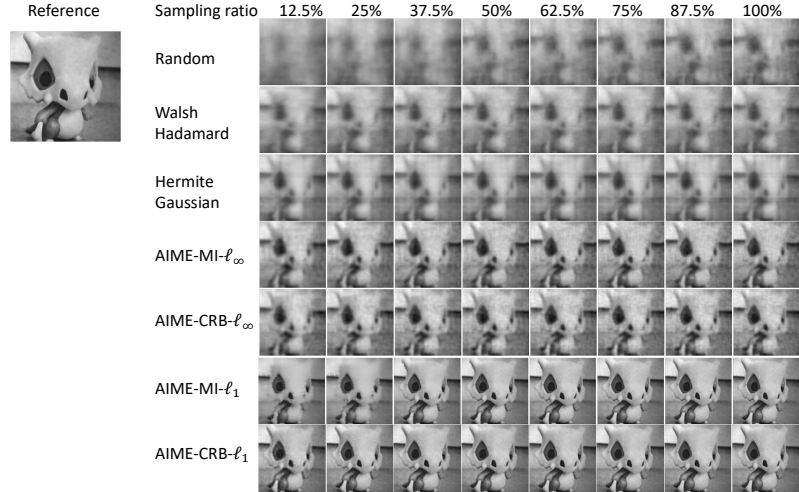


**Fig. A5:** Experimental imaging results of scene 1 under different sampling ratios for comparing GI with AIME and existing encoding patterns.

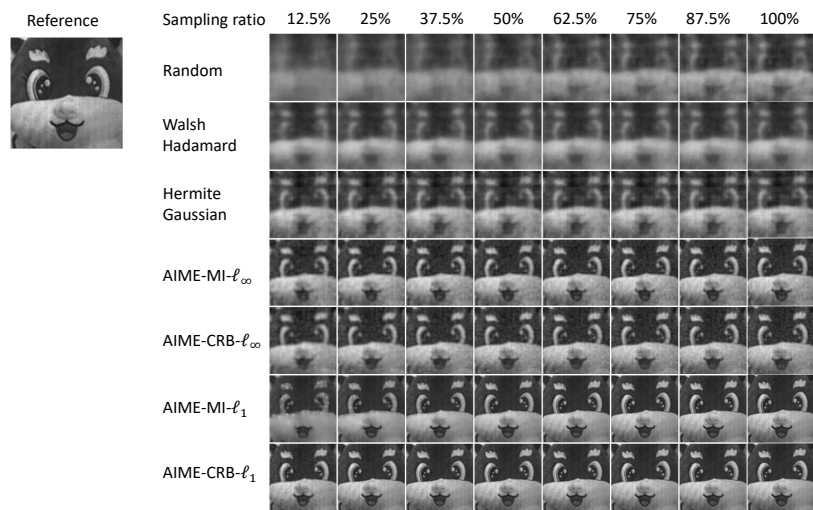


**Fig. A6:** Experimental imaging results of scene 2 under different sampling ratios for comparing GI with AIME and existing encoding patterns.

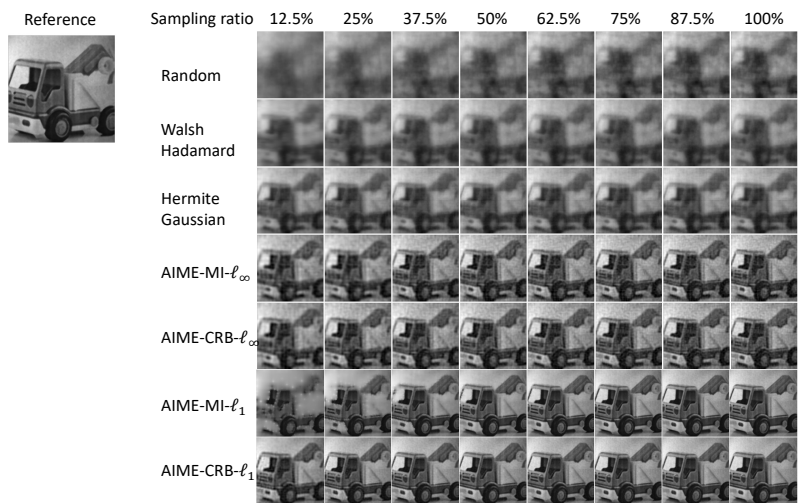


**Fig. A7:** Experimental imaging results of scene 3 under different sampling ratios for comparing GI with AIME and existing encoding patterns.

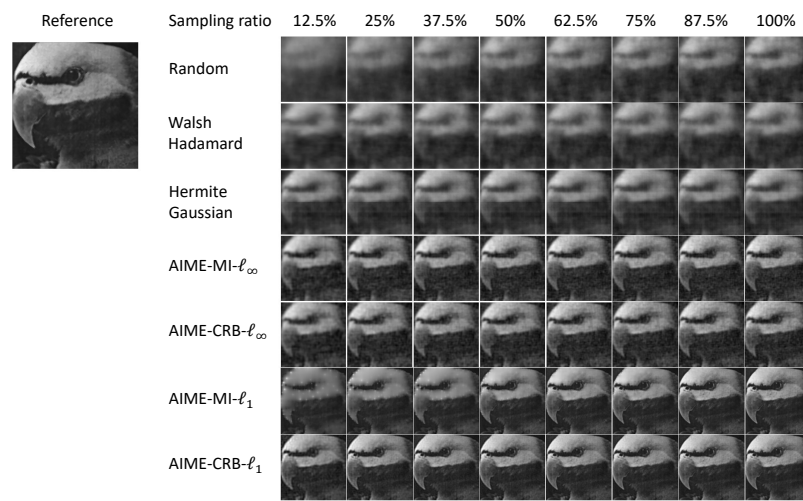


**Fig. A8:** Experimental imaging results of scene 4 under different sampling ratios for comparing GI with AIME and existing encoding patterns.

## Appendix F Information-optimal encoding under different SNRs

Figures A9 and A10 show AIME results under three different SNRs, which indicates that AIME can adaptively deal with different imaging conditions and constraints.

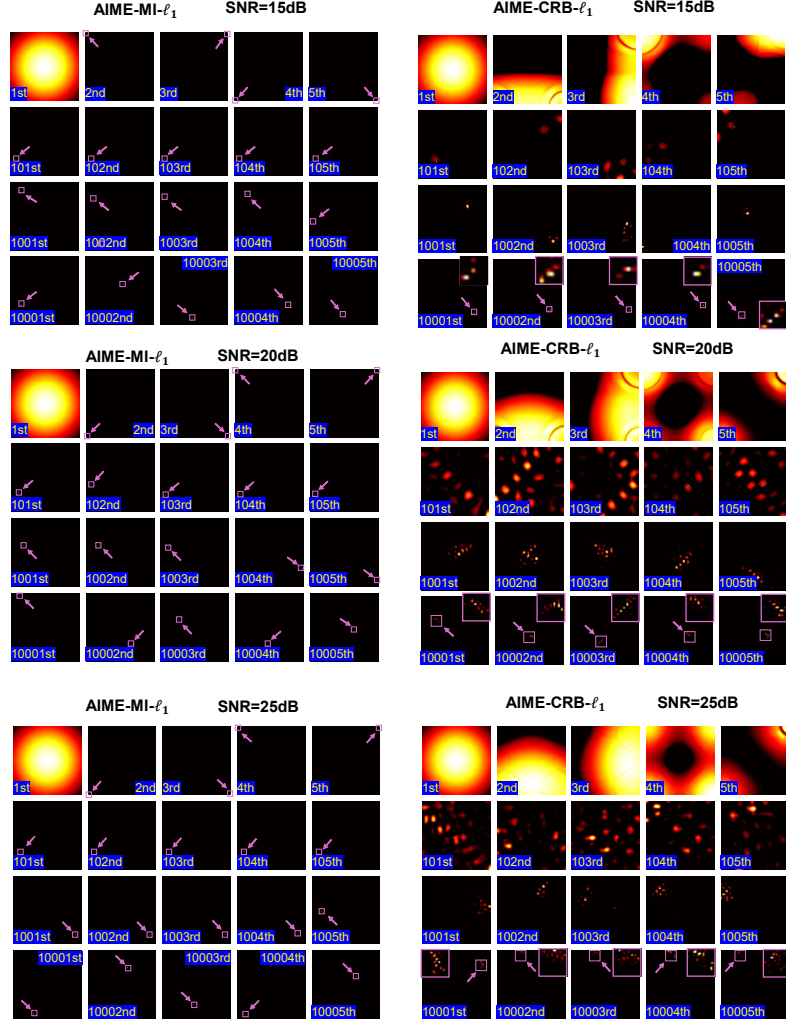


**Fig. A9:** Information-optimal encoding from AIME- $\ell_1$  under three different SNRs.

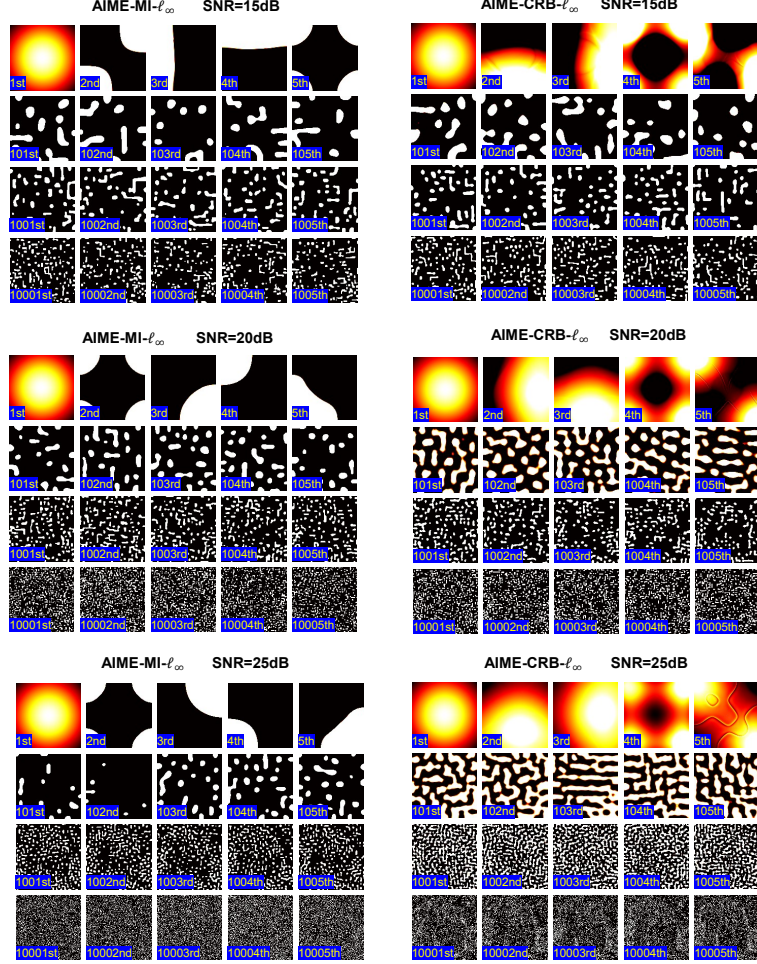


**Fig. A10:** Information-optimal encoding from AIME- $\ell_\infty$  under three different SNRs.

## References

- [1] Moreau, P.-A., Toninelli, E., Gregory, T., Padgett, M.J.: Ghost imaging using optical correlations. *Laser & Photonics Reviews* **12**(1), 1700143 (2018)
- [2] Eshun, A., Davenport, D., Demory, B., Kiannejad, S., Mos, P., Lin, Y., Bond, T., Rushford, M.C., Nuccio, E.E., Samo, T.J., *et al.*: 3d quantum ghost imaging microscope. *Optica* **12**(7), 1109–1112 (2025)
- [3] Tong, Z., Liu, Z., Wang, J., Shen, X., Han, S.: Breaking rayleigh's criterion via discernibility in high-dimensional light-field space with snapshot ghost imaging. arXiv preprint arXiv:2004.00135 (2020)

- [4] Tong, Z., Hu, C., Wang, J., Zhu, Y., Shen, X., Liu, Z., Han, S.: Single-shot super-resolution imaging via discernibility in the high-dimensional light-field space based on ghost imaging. *Photonics Research* **13**(6), 1709–1725 (2025)
- [5] Yuan, X., Han, S.: Single-pixel neutron imaging with artificial intelligence: Breaking the barrier in multi-parameter imaging, sensitivity, and spatial resolution. *The Innovation* **2**(2) (2021)
- [6] Hu, C., Tong, Z., Liu, Z., Huang, Z., Wang, J., Han, S.: Optimization of light fields in ghost imaging using dictionary learning. *Optics Express* **27**(20), 28734–28749 (2019)
- [7] Deng, C., Pan, L., Wang, C., Gao, X., Gong, W., Han, S.: Performance analysis of ghost imaging lidar in background light environment. *Photonics Research* **5**(5), 431–435 (2017)
- [8] Pan, L., Wang, Y., Deng, C., Gong, W., Bo, Z., Han, S.: Micro-doppler effect based vibrating object imaging of coherent detection gisc lidar. *Optics Express* **29**(26), 43022–43031 (2021)
- [9] Liu, S., Liu, Z., Hu, C., Li, E., Shen, X., Han, S.: Spectral ghost imaging camera with super-rayleigh modulator. *Optics Communications* **472**, 126017 (2020)
- [10] Chu, C., Liu, S., Liu, Z., Hu, C., Zhao, Y., Han, S.: Spectral polarization camera based on ghost imaging via sparsity constraints. *Applied Optics* **60**(16), 4632–4638 (2021)
- [11] Li, W., Tong, Z., Xiao, K., Liu, Z., Gao, Q., Sun, J., Liu, S., Han, S., Wang, Z.: Single-frame wide-field nanoscopy based on ghost imaging via sparsity constraints. *Optica* **6**(12), 1515–1523 (2019)
- [12] Chen, L., Wang, P., Liu, Z., Wu, J., Han, S.: Multicolor super-resolution structured illumination microscopy based on snapshot spectral ghost imaging via sparsity constraints. *ACS Photonics* **12**(7), 3565–3573 (2025)
- [13] Zhang, A.-X., He, Y.-H., Wu, L.-A., Chen, L.-M., Wang, B.-B.: Tabletop x-ray ghost imaging with ultra-low radiation. *Optica* **5**(4), 374–377 (2018)
- [14] He, Y.-H., Huang, Y.-Y., Zeng, Z.-R., Li, Y.-F., Tan, J.-H., Chen, L.-M., Wu, L.-A., Li, M.-F., Quan, B.-G., Wang, S.-L., *et al.*: Single-pixel imaging with neutrons. *Science Bulletin* **66**(2), 133–138 (2021)
- [15] Stantchev, R.I., Yu, X., Blu, T., Pickwell-MacPherson, E.: Real-time terahertz imaging with a single-pixel detector. *Nature communications* **11**(1), 2535 (2020)
- [16] Bogdanov, S., Preimesberger, A., Mishra, H., Hornof, D., Spielauer, T., Thajer, F., Maurer, M., Falb, P., Stöger, L., Schachinger, T., *et al.*: Ghost imaging with

free electron-photon pairs. arXiv preprint arXiv:2509.14950 (2025)

- [17] Wu, X., Zhou, C., Li, B., Huang, J., Meng, Y., Song, L., Han, S.: Image-free cross-species pose estimation via an ultra-low sampling rate single-pixel camera. *Chinese Optics Letters* **23**(9), 091101 (2025)
- [18] Abbas, A., Mu, J., Mengyue, Z., Cao, J., Zhang, X.: Target recognition in ghost imaging from traditional to advance; a brief review. *Optics & Laser Technology* **184**, 112450 (2025)
- [19] Barrett, H.H., Myers, K.J.: *Foundations of Image Science*. John Wiley & Sons, Hoboken, NJ, USA (2013)
- [20] Shensheng, H., Chenyu, H.: Review, current status and prospect of researches on information optical imaging. *Infrared and Laser Engineering* **51**(1), 20220017–1 (2022)
- [21] Hu, C., Han, S.: On ghost imaging studies for information optical imaging. *Applied Sciences* **12**(21), 10981 (2022)
- [22] Li, E., Chen, M., Gong, W., Yu, H., Han, S.: Mutual information of ghost imaging systems. *Acta Optica Sinica* **33**(12), 1211003 (2013)
- [23] Li, J., Luo, B., Yang, D., Yin, L., Wu, G., Guo, H.: Negative exponential behavior of image mutual information for pseudo-thermal light ghost imaging: observation, modeling, and verification. *Science Bulletin* **62**(10), 717–723 (2017)
- [24] Hu, C., Zhu, R., Yu, H., Han, S.: Correspondence fourier-transform ghost imaging. *Physical Review A* **103**(4), 043717 (2021)
- [25] Wei, X.-X., Stocker, A.A.: Mutual information, fisher information, and efficient coding. *Neural Computation* **28**(2), 305–326 (2016)
- [26] Blahut, R.E.: *Principles and Practice of Information Theory*. Addison-Wesley Longman Publishing Co., Inc., Reading, MA, USA (1987)
- [27] Fisher, R.A.: On the mathematical foundations of theoretical statistics. *Philosophical transactions of the Royal Society of London. Series A, containing papers of a mathematical or physical character* **222**(594-604), 309–368 (1922)
- [28] Eldar, Y.C., Kutyniok, G.: *Compressed Sensing: Theory and Applications*. Cambridge University Press, Cambridge, UK (2012)
- [29] Xu, X., Li, E., Shen, X., Han, S.: Optimization of speckle patterns in ghost imaging via sparse constraints by mutual coherence minimization. *Chinese Optics Letters* **13**(7), 071101 (2015)
- [30] Czajkowski, K.M., Pastuszczak, A., Kotyński, R.: Single-pixel imaging with

morlet wavelet correlated random patterns. *Scientific Reports* **8**(1), 466 (2018)

[31] Tropp, J.A.: Greed is good: Algorithmic results for sparse approximation. *IEEE Transactions on Information theory* **50**(10), 2231–2242 (2004)

[32] Arias-Castro, E., Eldar, Y.C.: Noise folding in compressed sensing. *IEEE Signal Processing Letters* **18**(8), 478–481 (2011)

[33] Du, L.-K., Hu, C., Nie, Z.-W., Chang, C., Sun, S., Liu, S., Deng, C., Bo, Z., Liu, W.-T., Han, S.: Information-quantitative evaluation of linear computational imaging and application in ghost imaging. *Optics & Laser Technology* **192**, 113893 (2025)

[34] Wu, H., Wang, R., Huang, Z., Xiao, H., Liang, J., Wang, D., Tian, X., Wang, T., Cheng, L.: Online adaptive computational ghost imaging. *Optics and Lasers in Engineering* **128**, 106028 (2020)

[35] Wang, D., Liu, B., Song, J., Wang, Y., Shan, X., Zhong, X., Wang, F.: Dual-mode adaptive-svd ghost imaging. *Optics Express* **31**(9), 14225–14239 (2023)

[36] Donoho, D.L.: Compressed sensing. *IEEE Transactions on information theory* **52**(4), 1289–1306 (2006)

[37] Arias-Castro, E., Candes, E.J., Davenport, M.A.: On the fundamental limits of adaptive sensing. *IEEE Transactions on Information Theory* **59**(1), 472–481 (2012)

[38] Malloy, M.L., Nowak, R.D.: Near-optimal adaptive compressed sensing. *IEEE Transactions on Information Theory* **60**(7), 4001–4012 (2014)

[39] Huang, G., Shuai, Y., Ji, Y., Zhou, X., Li, Q., Liu, W., Gao, B., Liu, S., Liu, Z., Li, Y.: Compressed hermite–gaussian differential single-pixel imaging. *Applied Physics Letters* **124**(11) (2024)

[40] Candes, E.J., Romberg, J., Tao, T.: Robust uncertainty principles: exact signal reconstruction from highly incomplete frequency information. *IEEE Transactions on Information Theory* **52**(2), 489–509 (2006)

[41] Huang, X., Nan, S., Tan, W., Bai, Y., Fu, X.: Ghost imaging for detecting trembling with random temporal changing. *Optics Letters* **45**(6), 1354–1357 (2020)

[42] Huang, X., Nan, S., Tan, W., Bai, Y., Fu, X.: Ghost imaging influenced by a supersonic wind-induced random environment. *Optics Letters* **46**(5), 1009–1012 (2021)

[43] Liu, Z., Yang, B., Zhang, Y., Shen, J., Yuan, X., Chen, M.K., Liu, F., Geng, Z.: Comprehensive compensation of real-world degradations for robust single-pixel

imaging. *Light: Science & Applications* **14**(1), 365 (2025)

- [44] Liu, Z., Tan, S., Wu, J., Li, E., Shen, X., Han, S.: Spectral camera based on ghost imaging via sparsity constraints. *Scientific Reports* **6**(1), 25718 (2016)
- [45] Hyvärinen, A., Hurri, J., Hoyer, P.O.: *Natural Image Statistics: A Probabilistic Approach to Early Computational Vision.* vol. 39. Springer, New York, NY, USA (2009)
- [46] Elata, N., Michaeli, T., Elad, M.: Adaptive compressed sensing with diffusion-based posterior sampling. In: *European Conference on Computer Vision*, pp. 290–308 (2024). Springer
- [47] Pinkard, H., Kabuli, L., Markley, E., Chien, T., Jiao, J., Waller, L.: Information-driven design of imaging systems. *arXiv preprint arXiv:2405.20559* (2024)
- [48] Torralba, A., Oliva, A.: Statistics of natural image categories. *Network: Computation in Neural Systems* **14**(3), 391 (2003)
- [49] Schaible, S.: Fractional programming. ii, on dinkelbach's algorithm. *Management science* **22**(8), 868–873 (1976)